DOI: 10.1002/chem.200701053

Surfactant-Free Synthesis of Hyperbranched Monoclinic Bismuth Vanadate and its Applications in Photocatalysis, Gas Sensing, and Lithium-Ion Batteries

Yu Zhao, Yi Xie,* Xi Zhu, Si Yan, and Sunxi Wang[a]

Abstract: Hyperbranched monoclinic $BiVO_4$ (h-$BiVO_4$) has been synthesized on a large scale and with good uniformity by a surfactant-free hydrothermal route. h-$BiVO_4$ consists of four trunks with branches distributed on opposite sides. From observation of the intermediates at an early stage of the reaction process, it can be seen that during formation h-$BiVO_4$ has different growth rates along the *a*, *b*, and *c* axes. Based on crystal structure analysis and experimental results, h-$BiVO_4$ shows preferential growth along the [100] direction, and subsequently, along the [010] and [001] directions. As-synthesized h-$BiVO_4$ exhibits excellent photocatalytic ability in the photodegradation reaction of an aqueous solution of RB under visible light. Electrochemical measurements predict that h-$BiVO_4$ possesses high sensitivity to formaldehyde and ethanol gases, favorable discharge capacity, and capacity retention, which indicate potential applications in the fields of sensing devices and lithium-ion batteries.

Keywords: bismuth vanadates · hyperbranching · lithium-ion batteries · photochemistry · sensors

Introduction

Outside the realm of biology, some of the most beautiful and familiar examples of spontaneous pattern formation in nature can be found in the growth of crystals. Investigation into the chemical systems of these attractive crystal structures has shown that the distinctive size, shape, and chemical functionality of such structures make them promising candidates for the design and fabrication of new functional materials.[1] One example of these attractive patterns, the hyperbranched structure, is common in nature across a wide range of size scales.[2] Hyperbranched crystals usually have hexagonal or cubic symmetry, and have been obtained through different strategies, such as spontaneous ordered aggregation[3] and surfactant/ligand-assisted processes.[4] For example, well-defined α-Fe_2O_3 dendritic fractals have been fabricated from the hydrolysis of a single iron complex precursor by using spontaneously self-assembled nanoscale building blocks,[3a] and PbS 3D dendritic nanostructures have been obtained through a surfactant/ligand-assisted hydrothermal method.[4a] However, hyperbranched materials with low crystal symmetry (for instance, monoclinic) are not common in nature. To the best of our knowledge, the fabrication of hyperbranched structures of such materials without the assistance of templates, microemulsions, surfactant micelles, and so on, has seldom been reported to date. Thus, a challenge remains for material scientists to find simple and reliable methods for the controlled synthesis of hierarchically hyperbranched architectures of low crystal-symmetry materials with designed chemical components and expected functionalities.

Over the past few decades considerable attention has been devoted to metal-oxide semiconductors, which have extremely important applications in various fields, such as gas sensing,[5] lithium-ion batteries,[6] and photocatalysis.[7] One member of the Aurivillius family of layered oxides, monoclinic bismuth vanadate (m-$BiVO_4$) has attracted considerable attention as a result of its properties. This compound, which has important applications in pigments,[8] ionic conductivity,[9] and ferroelasticity,[10] also has the ability to photocatalytically split H_2O into O_2 and H_2 from an aqueous solution of $AgNO_3$[11d] and can photodegrade organic pollutants under visible-light irradiation.[11a–c] These novel photochemical properties make m-$BiVO_4$ a promising functional material with considerable potential applications in

[a] Dr. Y. Zhao, Prof. Y. Xie, X. Zhu, S. Yan, S. Wang
Department of Nanomaterials and Nanochemistry
Hefei National Laboratory for Physical Sciences at Microscale
University of Science and Technology of China
Hefei, Anhui, 230026 (P.R. China)
Fax: (+86) 551-360-3987
E-mail: yxie@ustc.edu.cn

Supporting information for this article is available on the WWW under http://www.chemeurj.org/ or from the author.

solving the energy and environmental issues that confront mankind today. Traditional methods for synthesizing m-$BiVO_4$ usually involve solid-state or melting reactions at high temperatures.[12] It would be of interest if a preparation method that controls the crystal forms under mild conditions could be developed. Recent advances have shown that m-$BiVO_4$ can be readily synthesized through a hydrothermal process.[11] The benefits of this method are the relatively low temperature required, environmentally friendly reaction conditions, and controllable morphology and size distribution.

Herein, we report the synthesis of m-$BiVO_4$ with a hyperbranched structure without the assistance of surfactants. Hyperbranched monoclinic $BiVO_4$ (h-$BiVO_4$) has been synthesized by the hydrothermal treatment of $Bi(NO_3)_3$ and $NaVO_4$ under acidic conditions. The structure is formed as a result of fast growth along the [100] direction and relatively slow growth along the [010] direction. h-$BiVO_4$ exhibits better photocatalytic ability when compared with hierarchical m-$BiVO_4$ frameworks, which were synthesized by a surfactant-assisted route outlined previously.[11b] As an important metal oxide semiconductor with a layered structure, we have investigated the electrochemical behavior of m-$BiVO_4$ for potential applications in gas sensing and lithium-ion batteries. h-$BiVO_4$ shows a high sensitivity to ethanol and formaldehyde gases, favorable discharge capacity, and capacity retention, which indicates that h-$BiVO_4$ represents an advanced material for building microdevices with predictable functionalities. This work could be of great importance for the exploration and expansion of potential applications of m-$BiVO_4$.

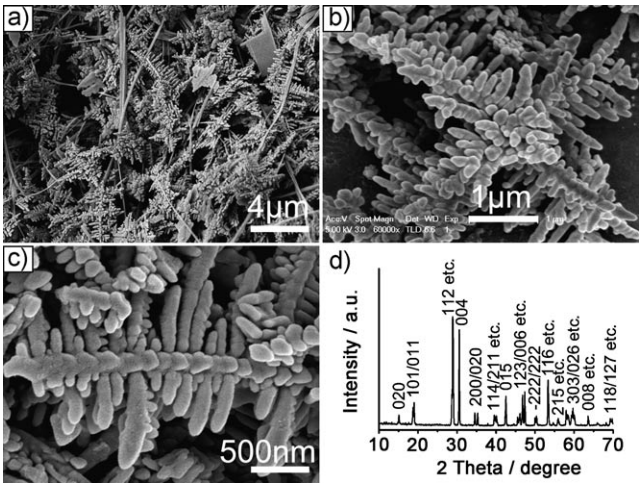

Figure 1. a) A representative FESEM image of the hyperbranched m-$BiVO_4$. b) A magnified FESEM image that shows a single hyperbranch of h-$BiVO_4$. c) A magnified FESEM image that shows the trunk of h-$BiVO_4$. d) The XRD pattern of h-$BiVO_4$.

Results and Discussion

Figure 1 shows the field-emission scanning electron microscopy (FESEM) images and XRD pattern of the synthesized product. A panoramic morphology of the product is presented in Figure 1a that reveals the hyperbranched structure and indicates a high yield. A magnified FESEM image that shows an individual h-$BiVO_4$ architecture is presented in Figure 1b. The hyperbranched structure grows with four pronounced trunks, which have corrugations and ordered branches that are symmetrically distributed on opposite sides of the trunks. The length of the trunks is 3 to 5 μm, whereas the length of the branches ranges from 200 to 500 nm. Figure 1c shows a magnified FESEM image of an individual trunk. All of the branches have a similar structure and opposing directions of protrusion. It is also worth noting that there are some protuberances, rather than branches, that grow perpendicular to both the trunk and the branches. Figure 1d shows the XRD pattern of h-$BiVO_4$. All of the diffraction peaks can be indexed as a monoclinic lattice (space group $I2/b$) of $BiVO_4$ with cell constants of $a=5.200$, $b=5.097$, and $c=11.74$ Å, which are consistent with the values given by the Joint Committee on Powder Diffraction Standards (JCPDS 83-1700). No peaks for other phases or impurities were detected, which indicated the high purity of the product.

Figure 2 shows transmission electron microscopy (TEM) and high-resolution transmission electron microscopy (HRTEM) images of h-$BiVO_4$ and the associated selective

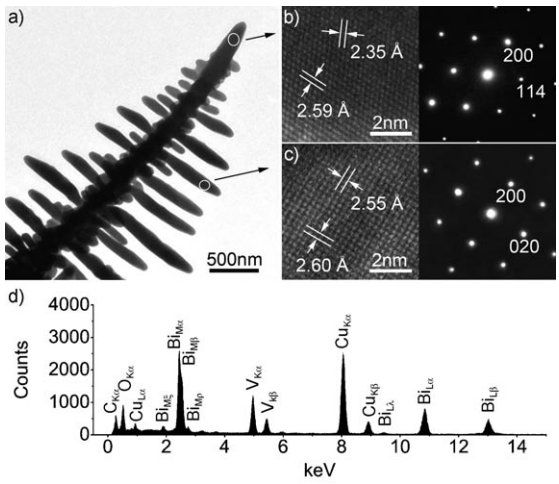

Figure 2. a) A TEM image of the trunk of an individual hyperbranch. b) and c) The HRTEM images (left) associated with the SAED patterns (right) of h-$BiVO_4$. d) The corresponding EDX pattern of h-$BiVO_4$.

area electron diffraction (SAED) and energy-dispersive X-ray spectroscopy (EDX) patterns. Figure 2a shows the TEM image of an individual trunk. Despite the fact that there are some shorter branches positioned between the normal-sized branches, in general the closer the branches are to the tip of the trunk the shorter they become. This phenomenon suggests that the growth rates of the trunks and the branches are clearly different. Figure 2b and c shows HRTEM images and SAED patterns of the trunk and branch, respectively, as

indicated in Figure 2a. The separations of 2.59 and 2.60 Å in Figure 2b and c, respectively, correspond to the distance between adjacent (200) crystal planes, whereas the separations of 2.35 (Figure 2b) and 2.55 Å (Figure 2c) correspond to the distance between adjacent (114) and (020) crystal planes, respectively. h-$BiVO_4$ shows fast growth along the [100] direction (the trunk) and subsequent growth along the [010] direction (the branch). In combination with the FESEM observations (Figure 1c), the results indicate that the growth rate along the [001] direction is much slower than along the [100] or [010] directions because no branches grow out from the trunk in this direction. Figure 2d shows the EDX spectrum of h-$BiVO_4$. Only bismuth, vanadium, and oxygen signals were observed (copper and carbon signals arise from the TEM grid), which indicates the high purity of the product. The ratio of Bi:V atoms is approximately 1:1.08, which is consistent with the stoichiometric ratio of $BiVO_4$.

Regarding the formation of h-$BiVO_4$, it is thought that protons play a key role because there are no other templates or organic additives in the reaction system. For a complete view of the morphology evolution, a detailed time-dependent study was conducted. Figure 3a to f shows a

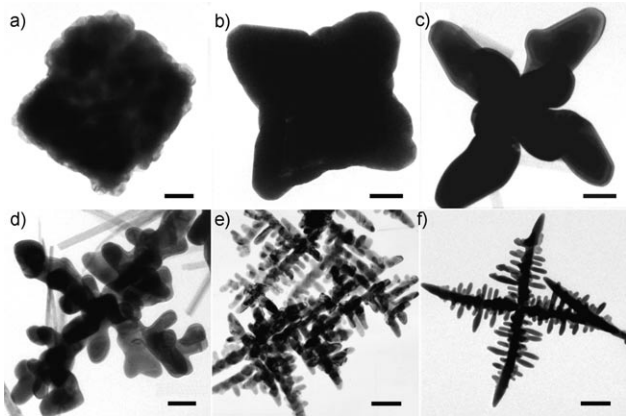

Figure 3. a)–f) A series of TEM images of the intermediate products collected at intervals of 10 min, 20 min, 30 min, 45 min, 1 h, and 3 h, respectively. The scale bars are 100, 200, 200, 200, 400 and 500 nm, respectively.

series of TEM images of the intermediates taken at intervals of 10 min, 20 min, 30 min, 45 min, 1 h and 3 h, respectively, after the reaction had begun. The intermediates clearly show a continuous morphology evolution from a square to a tetrapod-branched structure, and finally to a hyperbranched structure. After the reaction had proceeded for 10 min, square particles were generated and after 30 min the intermediates had grown bigger and became tetrapod-branched structures. As the reaction time increased to 3 h, branches grew out of the trunks. For reaction times of 6 h, the product consisted predominantly of h-$BiVO_4$. Accompanying XRD analysis indicated that the intermediates were phase-pure m-$BiVO_4$ (see the Supporting Information). To understand why protons seriously affected the formation of the hyperbranched structure, we first considered the crystal structure of m-$BiVO_4$.[11a] Figure 4a (left–right) shows the side elevation of the {100}, {010}, and {001} facets, respectively. The V–O polyhedrons (VOPs) and Bi–O polyhedrons (BOPs)

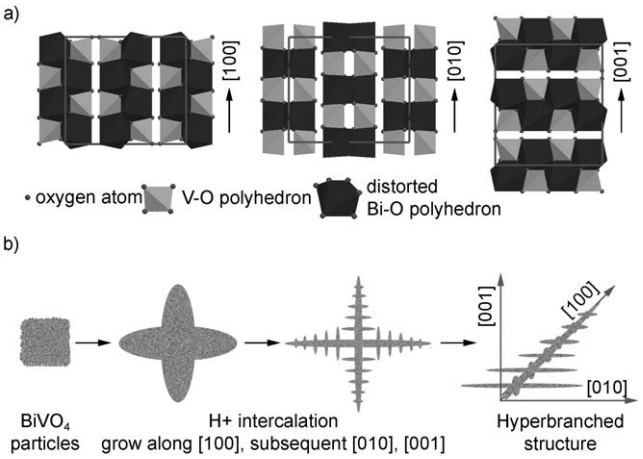

Figure 4. a) Side elevation views of the {100}, {010} and {001} facets (left–right) of a $2\times2\times1$ section of m-$BiVO_4$. b) A schematic illustration of the formation process of the hyperbranched structure.

are closely packed along the [100] direction (Figure 4a, left), whereas along the [010] direction they are less closely packed and have aligned tunnels (Figure 4a, center). We believe that these aligned tunnels facilitate the dissolution of $BiVO_4$ in strongly acidic conditions (pH 2–3) because there is enough space for protons to intercalate into the tunnels. As the intercalation of protons and the dissolution process occurs, the growth rate along the [010] direction slows down. However, in comparison, the growth rate along the [100] direction is not as seriously affected by proton intercalation because of the closely packed VOPs and BOPs. Therefore, the [100] direction becomes the preferential orientation direction. The m-$BiVO_4$ crystal has layers arranged in a lamellar structure along the [001] direction (Figure 4a, right). The space between these neighboring layers favors the proton-intercalation-induced dissolution process. Therefore, the growth rate along the [001] direction is rapidly decelerated, and instead of branches, only protuberances grow out of the trunk. This proton-induced dissolution process for the generation of micro- and nanostructures has also been observed in the synthesis of metal-oxide-based materials, such as α-Fe_2O_3 nanotubes,[13] ammonium molybdenum/tungsten bronze nanorods,[14] and vanadium pentoxide nanobelts,[15], which are a result of acidity during formation and are closely related to the crystal structure. Based on the time-dependent morphology evolution evidence and the crystal structure analysis, a proton-induced dissolution process for the formation of h-$BiVO_4$ has been proposed. A schematic illustration of this process is presented in Figure 4b.

Although the hyperbranched-formation process has been deduced, direct evidence of the shape transformation caused by proton intercalation and dissolution cannot be proved.

To confirm the key role that protons play in this formation process, we conducted a series of parallel experiments to indirectly verify the rationality of our proposed formation process. Figure 5a to d shows the products obtained at different

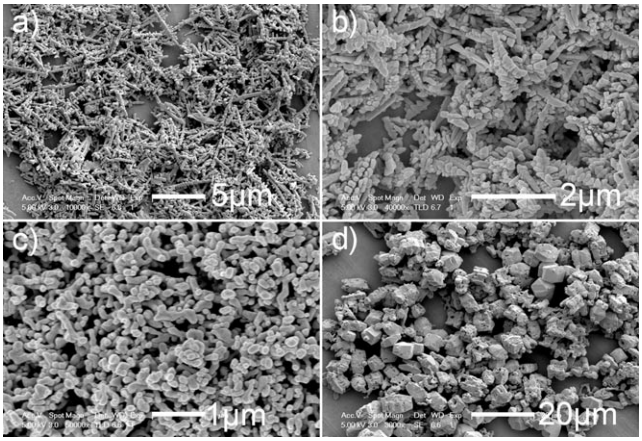

Figure 5. a)–d) FESEM images of the products obtained at pH values of 1.0, 4.0, 6.0 and 8.0, respectively.

pH values (1.0, 4.0, 6.0, and 8.0, respectively). XRD analysis has confirmed the monoclinic lattice of $BiVO_4$ (see the Supporting Information). As the pH value decreases from between 2.0 and 3.0 to 1.0, the product appears to be rodlike and the branches are shortened (Figure 5a), which indicates that the proton intercalation and dissolution process becomes more intense. The tunnels aligned along the [010] direction are more likely to be attacked by protons, and therefore, the growth rate along the [010] direction slows down, which results in the formation of shortened branches (compared with h-$BiVO_4$). As the pH value increases from between 2.0 and 3.0 to 4.0, the product appears to be grapelike (see Figure 5b). Shorter branches are aligned around the trunk and the length of the branches in different directions is indistinguishable. This result suggests that as the proton concentration decreases, the intercalation and dissolution process is weakened and the growth rate along the [010] and [001] directions are evenly matched. However, the ruling growth direction is still along the [100] direction. As the pH value is increased to 6.0 and then 8.0, only particles can be distinguished (Figure 5c and d, respectively). The increased pH value leads to a decreased intensity of proton intercalation and dissolution, and therefore, no specific morphology apart from particles can be obtained.

Photodegradation of H_2O and organic pollutants with photocatalysts is promising as a method to solve the urgent energy and environmental issues that confront mankind today. In prior research some UV-light-driven photocatalysts, TiO_2 for instance, have been extensively studied.[16] However, UV light makes up only 4% of the total solar energy emissions compared with visible light, which accounts for 43%. Therefore, the development of visible-light-driven photocatalysts with high-energy-transfer efficiency, low toxicity, and low cost for industrial production has become one of the most challenging tasks. The photocatalytic performance of h-$BiVO_4$ was tested on the photodegradation of *N*,*N*,*N*′,*N*′-tetraethylated rhodamine B (RB) under visible-light irradiation. The UV/Vis diffuse reflectance spectrum of h-$BiVO_4$ is shown in Figure 6a. h-$BiVO_4$ shows a strong absorption in the visible-light region in addition to that in the UV-light region. The energy of the band gap of h-$BiVO_4$ can be obtained from a plot of $(\alpha h\nu)^2$ versus photon energy ($h\nu$; Figure 6a, inset). The value estimated from the x axis intercept of the tangent is 2.3 eV, which is consistent with previous reports.[11d,17] Figure 6b shows the decrease in UV/Vis absorption intensity of the solution of RB with time, recorded at 15 min intervals. The photodegradation rate is over 90% after 45 min under visible-light irradiation. We also used commercial TiO_2 (commercial Degussa P25 TiO_2) and dense bulk m-$BiVO_4$ particles (Figure 5d) as references to evaluate the photocatalytic performance of h-$BiVO_4$. As illustrated in the inset of Figure 6b, it is obvious that h-$BiVO_4$ exhibits superior photocatalytic abilities over P25 and dense bulk m-$BiVO_4$ particles. Moreover, h-$BiVO_4$ exhibits better photodegradation efficiency compared with the m-$BiVO_4$ hierarchical frameworks of our previous report.[11b] We assume that the surfactant-free reaction system is responsible for the enhancement of photode-

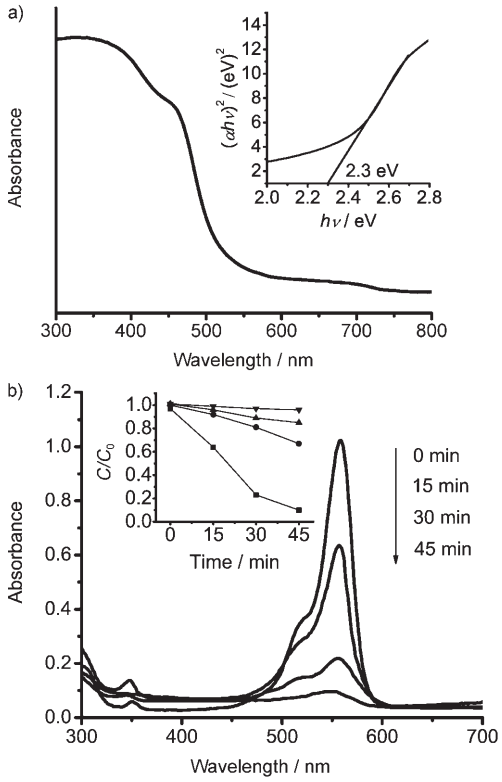

Figure 6. a) The UV/Vis diffuse reflectance spectra of h-$BiVO_4$. Inset: A plot of $(\alpha h\nu)^2$ vs. photon energy ($h\nu$). b) Changes to the UV/Vis spectrum of an aqueous solution of RB as a function of irradiation time. Inset: Comparison of the change in RB concentration under different catalytic conditions; ▼ = photocatalyst-free solution, ▲ = P25, ● = dense bulk m-$BiVO_4$ particles, and ■ = h-$BiVO_4$.

gradation efficiency. Generally, the activity of a photocatalyst increases with an increase in surface area, not only because the photocatalytic reaction usually takes place on the surface, but also because the efficiency of the electron–hole separation is promoted.[18] The complete removal of surfactant is a complicated process and there is a considerable chance of organic molecules being adsorbed onto the surface, which would prevent direct contact with pollutant molecules and decrease the photodegradation efficiency.

The electrochemical behavior of m-$BiVO_4$ is of concern when considering the fact that it is a metal-oxide semiconductor with a layered structure. Herein, the applications of h-$BiVO_4$ in gas sensing and lithium-ion batteries were investigated. Sensing devices based on metal-oxide semiconductors are mainly used for the detection of combustible and noxious gases. When a metal-oxide semiconductor is exposed to reducing or oxidizing gases, its resistance varies in accordance with the gas concentration. The theory for the operation of such sensors involves adsorption/desorption phenomena and reactions at the surface of the metal oxide.[5a] The gas sensitivity is defined as the resistance ratio R_{air}/R_{gas}, in which R_{air} and R_{gas} are the electrical resistances for the sensor in air and gas, respectively. The sensing properties of h-$BiVO_4$ towards trace levels of gas were analyzed at room temperature in dry air. Figure 7 shows the room temperature gas-sensing characteristic of h-$BiVO_4$ (sensitivity vs. gas-vapor concentration) in response to ethanol and formaldehyde (curves a) and b), respectively) compared with dense bulk m-$BiVO_4$ particles (curves c) and d), respectively). The sensitivity of h-$BiVO_4$ increases with an increase in the concentration of ethanol or formaldehyde gas. However, the dense bulk m-$BiVO_4$ particles are less sensitive to the concentration of gas present. The sensitivity of h-$BiVO_4$ to the two gases is distinguishable even at a concentration of 10 ppm. The higher sensitivity of h-$BiVO_4$ can be attributed to the relatively large surface area compared with the dense bulk particles, which gives a better opportunity to adsorb and desorb gas molecules.[19] In our study, we found that the on and off responses for h-$BiVO_4$ can be repeated many times without observing major changes in the signal, which indicates stable reversibility and potential applications in combustible and noxious gas detection.

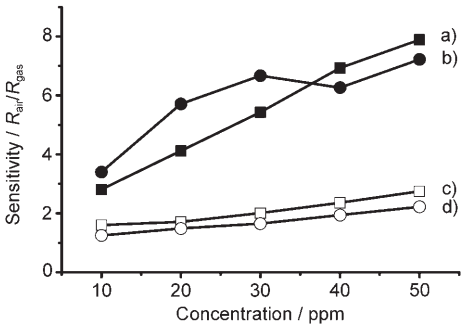

Figure 7. a) and b) The sensitivity (at RT) of h-$BiVO_4$ to ethanol (■) and formaldehyde (●), respectively. c) and d) The sensitivity (at RT) of dense bulk m-$BiVO_4$ particles to ethanol (□) and formaldehyde (○), respectively.

For years world-wide research has been focused on finding alternative anode materials for lithium-ion batteries to improve their energy density and safety.[20] It was found that 3D transition-metal oxides have enhanced reversible capacities compared with that of graphite.[21] The electrochemical behavior and layered structure of m-$BiVO_4$ facilitates the intercalation and deintercalation of lithium ions compared with the dense bulk materials, which is noteworthy in the field of rechargeable lithium-ion batteries. Figure 8 shows

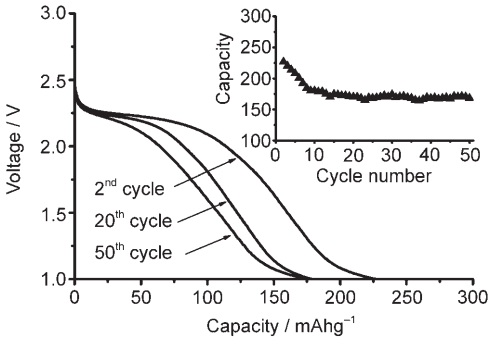

Figure 8. Voltage versus discharge capacity curves for the 2nd, 20th, and 50th cycles of an h-$BiVO_4$/Li cell between 2.5 and 1.0 V. Inset: The corresponding cyclic performance of the cell.

the voltage (2.5–1.0 V) versus discharge capacity curve for a cell (current density = 50 mA h g^{-1}, 293 K) for the 2nd, 20th, and 50th cycles. The discharge curve of the h-$BiVO_4$ electrode has a long plateau. The highest discharge capacity of the second cycle is 226.8 mAhg^{-1}, whereas the reversible discharge capacity after 50 cycles is 168.3 mA h g^{-1} (74% of the second discharge capacity). The inset of Figure 8 shows the cyclic performance of the h-$BiVO_4$ electrode. The relatively high discharge capacity and stable capacity retention indicate a potential application as a cathode material in lithium-ion batteries.

Conclusion

In conclusion, m-$BiVO_4$ with a hyperbranched structure has been successfully synthesized through a surfactant-free hydrothermal route. The dissolution process and the arrangement of VOPs and BOPs in the crystal result in different growth rates along the *a*, *b*, and *c* axes, therefore, a proton-induced intercalation–dissolution process for the formation of the hyperbranched structure has been proposed. h-$BiVO_4$ shows excellent visible-light driven photocatalytic ability in the photodegradation of RB in solution. The electrochemical behavior of h-$BiVO_4$ in gas sensing and in lithium-ion batteries was also investigated. The high sensitivity to ethanol and formaldehyde gases, and favorable discharge capaci-

ty and capacity retention, suggest that h-$BiVO_4$ has promising potential for application in these fields.

Experimental Section

All of the chemicals used were analytical reagents, purchased from Shanghai Chemical Company and used without further purification. In a typical procedure, $Bi(NO_3)_3{\cdot}5H_2O$ (240 mg, 0.50 mmol) was dissolved in distilled water (50 mL) and sonicated for 5 min to give a clear solution. Then $Na_3VO_4{\cdot}12H_2O$ (400 mg, 1.0 mmol) was added and stirred for 5 min to give an opaque solution. The pH value was then adjusted to approximately 2.0 to 3.0 with 2 M aqueous nitric acid before the solution was transferred to a Teflon-lined stainless steel autoclave with a capacity of 60 mL. The autoclave was heated to 473 K at a ramping rate of 5 K min^{-1} and maintained at 473 K for 6 h. After the autoclave cooled to room temperature, the bright yellow precipitate was collected, washed several times with distilled water and ethanol, and dried in a vacuum drying oven at 333 K for 6 h before characterization.

XRD patterns were recorded by using a Philips X'Pert Pro Super diffractometer with $Cu_{K\alpha}$ radiation ($\lambda = 1.54178$ Å), FESEM was performed by using an FEI Sirion-200 SEM, the TEM and HRTEM images associated with SAED and EDX analyses were performed by using a JEOL-2010 TEM with an acceleration voltage of 200 kV. The photocatalytic performance of h-$BiVO_4$ was evaluated by the degradation of RB under visible-light irradiation, which was provided by a Xenon lamp with a 380 nm cut-off filter. An aqueous suspension of $BiVO_4$ was prepared by adding powdered h-$BiVO_4$ (200 mg) to an aqueous solution of RB (100.0 mL, 5×10^{-5} M). The solution was protected from light and stirred for 6 h to reach adsorption equilibrium and uniform dispersion. At 15 min intervals after irradiation, the dispersion was filtered and the RB concentration of the filtrate was determined by using a UV/Vis-NIR spectrophotometer (Shimadzu SolidSpec-3700DUV). The same procedure was performed for P25 and dense bulk m-$BiVO_4$. Gas sensing measurements were performed at room temperature with a WS-30A system (Weisheng Instruments, Zhengzhou, China). The lithium-ion battery electrode experiments were carried out by using a Land battery system (CT2001A). The performance of h-$BiVO_4$ as a cathode was evaluated by using a Teflon cell with a lithium-metal anode. The cathode was a mixture of h-$BiVO_4$, acetylene black, and poly(vinylidene fluoride) with a weight ratio of 80:15:5. The electrolyte was 1 M $LiPF_6$ in ethylene carbonate/diethyl carbonate (1:1) and the separator was a Celgard 2320. The cell was assembled in a glove box filled with high-purity argon gas. The galvanostatic charge/discharge experiment was performed between 2.5 and 1.0 V at a constant discharge rate of 50 mAg^{-1} at 293 K.

Acknowledgements

This work was financially supported by the National Natural Science Foundation of China (20621061) and the State Key Project of Fundamental Research for Nanomaterials and Nanostructures (2005CB623601). The authors would like to acknowledge Mr. Linfeng Fei for his technical assistance.

[1] P. Yang, T. Deng, D. Zhao, P. Feng, D. Pine, B. F. Chmelka, G. M. Whitesides, G. D. Stucky, *Science* **1998**, *282*, 2244–2246.
[2] a) H. Yan, R. He, J. Pham, P. Yang, *Adv. Mater.* **2003**, *15*, 402–405; b) S. J. May, J. G. Zheng, B. W. Wessels, L. J. Lauhon, *Adv. Mater.* **2005**, *17*, 598–602; c) L. Manna, D. J. Milliron, A. Meisel, E. C. Scher, A. P. Alivisatos, *Nat. Mater.* **2003**, *2*, 382–385; d) J. Zhu, H. Peng, C. K. Chan, K. Jarausch, X. F. Zhang, Y. Cui, *Nano Lett.* **2007**, *7*, 1095–1099; e) J. P. Ge, J. Wang, H. X. Zhang, X. Wang, Q. Peng, Y. D. Li, *Chem. Eur. J.* **2005**, *11*, 1889–1894.
[3] a) M. Cao, T. Liu, S. Gao, G. Sun, X. Wu, C. Hu, Z. L. Wang, *Angew. Chem.* **2005**, *117*, 4269–4273; *Angew. Chem. Int. Ed.* **2005**, *44*, 4197–4201; b) Q. Peng, Y. Dong, Z. Deng, Y. Li, *Inorg. Chem.* **2002**, *41*, 5249–5254; c) F. Cheng, J. Zhao, W. Song, C. Li, H. Ma, J. Chen, P. Shen, *Inorg. Chem.* **2006**, *45*, 2038–2044; d) H. J. Fan, R. Scholz, F. M. Kolb, M. Zacharias, *Appl. Phys. Lett.* **2004**, *85*, 4142–4144.
[4] a) D. Kuang, A. Xu, Y. Fang, H. Liu, C. Frommen, D. Fenske, *Adv. Mater.* **2003**, *15*, 1747–1750; b) G. Zou, K. Xiong, C. Jiang, H. Li, T. Li, J. Du, Y. Qian, *J. Phys. Chem. B* **2005**, *109*, 18356–18360; c) Z. R. Tian, J. Liu, J. A. Voigt, H. Xu, M. J. Mcdermott, *Nano Lett.* **2003**, *3*, 89–92; d) X. Wang, K. Naka, H. Itoh, S. Park, Y. Chujo, *Chem. Commun.* **2002**, 1300–1301.
[5] a) N. Pinna, G. Neri, M. Antonietti, M. Niederberger, *Angew. Chem.* **2004**, *116*, 4445–4449; *Angew. Chem. Int. Ed.* **2004**, *43*, 4345–4349; b) G. Neri, A. Bonavita, G. Micali, G. Rizzo, S. Galvagno, M. Niederberger, N. Pinna, *Chem. Commun.* **2005**, 6032–6034.
[6] a) J. Chen, L. N. Xu, W. Y. Li, X. L. Gou, *Adv. Mater.* **2005**, *17*, 582–586; b) X. W. Lou, Y. Wang, C. Yuan, J. Y. Lee, L. A. Archer, *Adv. Mater.* **2006**, *18*, 2325–2329; c) A. M. Cao, J. S Hu, H. P. Liang, L. J. Wan, *Angew. Chem.* **2005**, *117*, 4465–4469; *Angew. Chem. Int. Ed.* **2005**, *44*, 4391–4395.
[7] a) M. R. Hoffmann, S. T. Martin, W. Choi, D. W. Bahnemann, *Chem. Rev.* **1995**, *95*, 69–96; b) G. Wang, W. Lu, J. Li, J. Choi, Y. Jeong, S. Y. Choi, J. B. Park, M. K. Ryu, K. Lee, *Small* **2006**, *2*, 1436–1439; c) M. Miyauchi, A. Nakajima, T. Watanabe, K. Hashimoto, *Chem. Mater.* **2002**, *14*, 2812–2816.
[8] H. Endriss in *High Performance Pigments*, (Ed. H. M. Smith), Wiley-VCH, Weinheim, Germany, **2002**, pp. 7–12.
[9] K. Hirota, G. Komatsu, M. Yamashita, H. Takemura, O. Yamaguchi, *Mater. Res. Bull.* **1992**, *27*, 823–830.
[10] Y. T. Yeom, S. H. Choh, M. L. Du, M. S. Jang, *Phys. Rev. B* **1996**, *53*, 3415–3421.
[11] a) L. Zhang, D. Chen, X. Jiao, *J. Phys. Chem. B* **2006**, *110*, 2668–2673; b) Y. Zheng, J. Wu, F. Duan, Y. Xie, *Chem. Lett.* **2007**, 36, 520–521; c) J. Yu, A. Kudo, *Adv. Funct. Mater.* **2006**, *16*, 2163–2169; d) A. Kudo, K. Omori, H. Kato, *J. Am. Chem. Soc.* **1999**, *121*, 11459–11467.
[12] a) R. S. Roth, J. L. Waring, *Am. Mineral.* **1963**, *48*, 1348–1356; b) A. W. Sleight, H. Y. Chen, A. Ferretti, *Mater. Res. Bull.* **1979**, *14*, 1571–1581.
[13] C. J. Jia, L. D. Sun, Z. G. Yan, L. P. You, F. Luo, X. D. Han, Y. C. Pang, Z. Zhang, C. H. Yan, *Angew. Chem.* **2005**, *117*, 4402–4407; *Angew. Chem. Int. Ed.* **2005**, *44*, 4328–4333.
[14] A. Michailovski, F. Krumeich, G. R. Patzke, *Chem. Mater.* **2004**, *16*, 1433–1440.
[15] B. Li, Y. Xu, G. Rong, M. Jing, Y. Xie, *Nanotechnology* **2006**, *17*, 2560–2566.
[16] a) A. L. Linsebigler, G. Lu, J. T. Yates, *Chem. Rev.* **1995**, *95*, 735–758; b) R. Asahi, T. Morikawa, T. Ohwaki, K. Aoki, Y. Taga, *Science* **2001**, *293*, 269–271.
[17] L. Zhou, W. Wang, S. Liu, L. Zhang, H. Xu, W. Zhu, *J. Mol. Catal. A* **2006**, *252*, 120–124.
[18] J. Tang, Z. Zou, J. Ye, *Chem. Mater.* **2004**, *16*, 1644–1649.
[19] a) C. J. Martinez, B. Hockey, C. B. Montgomery, S. Semancik, *Langmuir* **2005**, *21*, 7937–7944; b) Q. Zhao, Y. Gao, X. Bai, C. Wu, Y. Xie, *Eur. J. Inorg. Chem.* **2006**, 1643–1648.
[20] a) Y. Idota, T. Kubota, A. Matsufuji, Y. Maekawa, T. Miyasaka, *Science* **1997**, *276*, 1395–1397; b) J. M. Tarascon, M. Armand, *Nature* **2001**, *414*, 359–367.
[21] P. Poizot, S. Laruelle, S. Grugeon, L. Dupont, J. M. Tarascon, *Nature* **2000**, *407*, 496–499.

Received: July 10, 2007
Published online: November 21, 2007

